Published: Measurement Science and Technology **31**, p. 025901 (2020) DOI: 10.1088/1361-6501/ab4556

Novel broadband measurement technique on PCB cells for the field- and stress-dependent impedance in ferromagnetic wires

Yujie Zhao,[1)] Yunfei Wang,[1)] Diana Estevez,[1)] Faxiang Qin,[1)] Huan Wang,[1)] Xuefei Zheng,[1)] Dmitriy Makhnovskiy[1,2)], and Huaxin Peng,[1)]

[1]*Institute for Composites Science Innovation (InCSI), School of Materials Science & Engineering, Zhejiang University, 38 Zheda Road, Hangzhou, 310027, PR China.*

[2]*Sensing Materials Technology Ltd, 44 St. Michaels Close, Plymouth, Devon, PL1 4RX, United Kingdom.*

Abstract

The lack of broadband impedance measurements has restricted the potential capabilities of ferromagnetic wire composites which have been mainly evaluated through theoretical impedance calculated from existing models without considering wire domain microstructure. Here, we developed an accurate method for measuring the impedance of ferromagnetic wires in a wide frequency range from 100 kHz up to 15 GHz under magnetic and stress stimuli. The broadband measurements were ensured by a more accurate microwave calibration on the PCB cell extending the reference planes up to the wire sample ends and by compensating the sample waveguide properties using the phase unwrapping technique proposed in this work. In addition, a specially designed dogbone PCB measurement cell allowed both magneto-impedance and stress-impedance measurements efficiently transferring the tensile stress from cell to the wire sample fixed onto it. The measured wire impedance can be then recalculated into the surface impedance which constitutes the boundary condition in the antenna equation describing the microwave scattering properties of a wire. The developed approach will make it possible to build a practically predictive scattering theory in composite materials with embedded wire inclusions and thus their implementation in real-world applications such as remote stress monitoring.

Keywords: magneto-impedance, stress-impedance, ferromagnetic resonance, surface impedance, microwave scattering, antenna equation, microwave calibration, tensile strain, composite materials, remote stress monitoring.

E-mails:contact@sensmattech.co.uk.

Published: Measurement Science and Technology **31**, p. 025901 (2020) DOI: 10.1088/1361-6501/ab4556

Introduction

Since its re-discovery in 1994, the magneto-impedance (MI) effect which refers to the change in ac electrical impedance due to the application of a static magnetic field has been the focus of much research interest. Main studies have been conducted in glass-coated microwires, where the strongest MI effect was generally observed leading to the development of magnetic field/stress sensors at MHz frequencies [1-6] and microwave tunable composites incorporating such wire inclusions.[7-10] However, due to the lack of broadband measurements the microwave properties of microwire composites have been evaluated merely from the theoretical impedance calculated from existing models [8,10-12] without considering microscopic magnetic structure of wire inclusions. Such issue presents a limitation for realization of practical applications in such composites, e.g. in remote stress monitoring where a proper interpretation of the distribution of local stresses becomes imperative. The situation could be reversed by developing a predictive model via existing formalisms of electromagnetism of continuous media that includes the material constitutive parameters such as dielectric properties of the hosting medium and magnetic and conductive properties of wires. In this paper, we develop a robust measurement setup that allows determining the wire impedance in the presence of magnetic field and stress stimuli in a wide frequency range. The impedance obtained from the accurate measurements can be then recalculated into surface impedance delivering the boundary conditions required to calculate the composites microwave response using the antenna equation. Such strategy also enables to avoid the consideration of the complex magnetic structure of the wire, which restricts the accurate modelling of the impedance in a broad frequency range. Our results constitute the basis for the development of a scattering theory in free space that would allow the full certification of ferromagnetic microwires as a class of functional fillers for microwave applications.

Published: Measurement Science and Technology **31**, p. 025901 (2020) DOI: 10.1088/1361-6501/ab4556

Integration of the tensile stress and high-frequency impedance measurements

In attempt to implement high-frequency impedance measurements in the presence of tensile stress, one is confronted with contradictory requirements. On the one hand, a high-frequency excitation requires special waveguide conditions to ensure the impedance matching along the whole measurement track. On the other hand, standard waveguide or coaxial measurement techniques exclude any possibility of a controllable stress transfer to the wire sample. The measurement setup we propose in the present work (Fig. 1(a,b)), can be used both for the magneto-impedance (MI) and stress-impedance (SI) measurements. It comprises Z5.0 TN Zwick Roell stress machine 5 kN, Helmholtz magnetic coil, power amplifier, dogbone PCB measurement cell, PCB calibration cell, LaVISION optical camera for the strain control, and three Rohde&Schwarz devices: ZNB20 Vector Network Analyzer (VNA) 20 GHz 2-port, HMF 2550 Function Generator (FG), and HMC 8012 Digital Multimeter (DMM). Synchronous operation of VNA, FG, and DMM, connected by LAN to a PC, is controlled by a LabVIEW program. All the devices are mounted on the height-adjustable trolley to allow its relocation for different experimental arrangements.

Published: Measurement Science and Technology **31**, p. 025901 (2020) DOI: 10.1088/1361-6501/ab4556

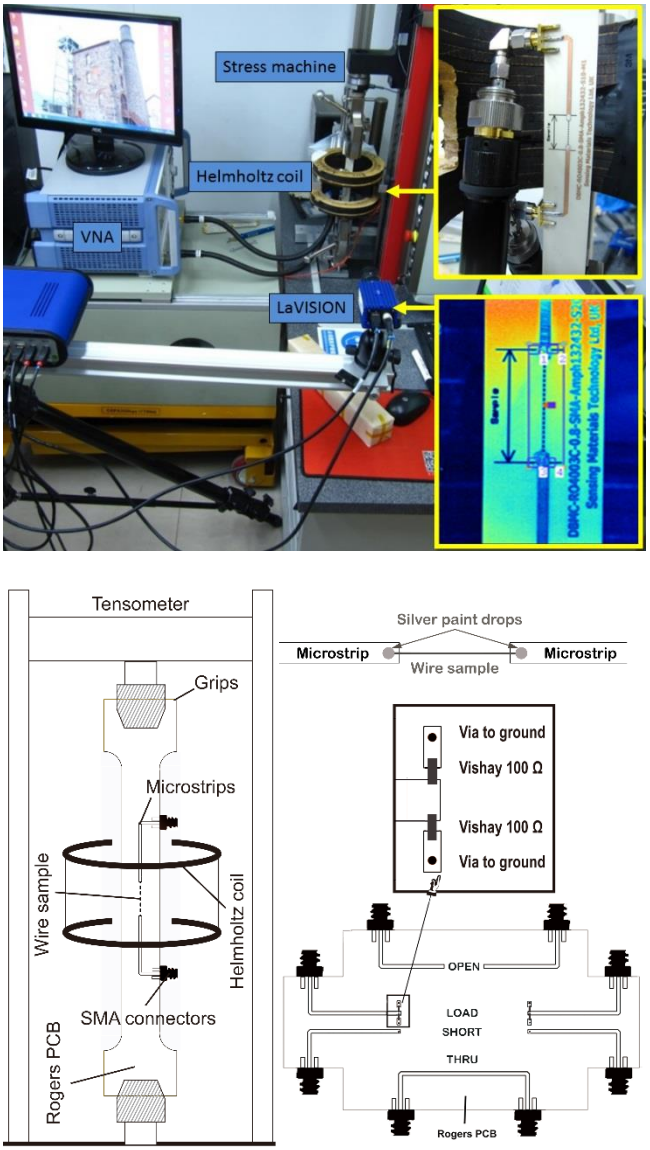

FIG. 1. Stress-impedance measurement setup (a) and its schematic diagram (b) showing the dogebone PCB measurement cell and the PCB calibration cell.

A dogbone PCB measurement cell has a continuous copper ground layer on one side of the board and the L-shape 50 Ω microstrips on the other one. The microstrips are terminated with SMA connectors which enabled coaxial cable connection with VNA. The wire sample is placed onto PCB in the gap between the microstrips (Fig. 1(b)) and connected to their ends by a

conductive silver paint. The dogbone shape of PCB and its ductility allow a graduate stress transfer from the machine grippers to the wire sample. We used Rogers' RO4003C material with the thickness 0.812 mm and the dielectric constant ~3.8 in a wide frequency range. The 1.78 mm width of microstrips, providing the 50 Ω characteristic impedance, was calculated using Rogers's microwave impedance calculator MWI 2017. The sample gap between the microstrips varied from 10 to 25 mm. A 2 mm space from the end of the microstrips was reserved for the wire electrical connection.

For accurate network measurements, it is necessary to propose a calibration technique that extends the reference planes from the cable coaxial connectors to the microstrip ends. We designed and built the PCB calibration cell realising SOLT calibration technique [13] in a wide frequency range from kHz up to 15 GHz. The PCB calibration cell, shown in Fig. 1(b), was made of the same RO4003C. The shape, length, and width of its microstrips must be identical to those on the dogbone PCB measurement cells. The SHORT and OPEN termination standards were made of the short grounded (through a via) and open microstrip ends respectively. The LOAD standard was made of two RF 100 Ω surface mounted resistors (Vishay resistor, size 0402) connected in parallel to the ground plane through the vias to provide the 50 Ω termination. Such configuration is used to reduce the parasitic inductance of the resistors. The THRU standard was made by connecting two microstrips together without the sample gap. When using this calibration cell with a VNA, the "ideal calibration kit" (option available in modern VNAs) can be chosen assuming that S_{11}-parameter (reflection coefficient) measured from SHORT, OPEN, and LOAD takes the values -1, 1, and 0 respectively. More realistic models for the SOL standards, considering their LC-paraments and delay times, could provide even better accuracy at higher GHz frequencies.

Published: Measurement Science and Technology **31**, p. 025901 (2020) DOI: 10.1088/1361-6501/ab4556

After the SOLT calibration on PCB, the reference plane will be shifted to the microstrips ends. The impedance Z of a wire sample placed onto PCB between the microstrips could be calculated from the measured transmission coefficient S_{21} using the well-known equation: $Z = 100 \times (1 - S_{21})/S_{21}$. However, this equation assumes that S_{21} is measured from a lumped element. This is not the case for a wire sample at the frequencies beyond a hundred of MHz because it represents by itself a waveguide over the ground plane. To extract purely impedance properties, the phase incursion along the sample caused by the wave propagation must be compensated. To do so, the phase of $S_{21}(\omega)$, measured through the wire sample at zero magnetic field and stress, was first unwrapped, see Fig. 2, and then approximated by a linear trend line $\omega a + b$ within a frequency interval where the phase has minimum non-linear distortions.

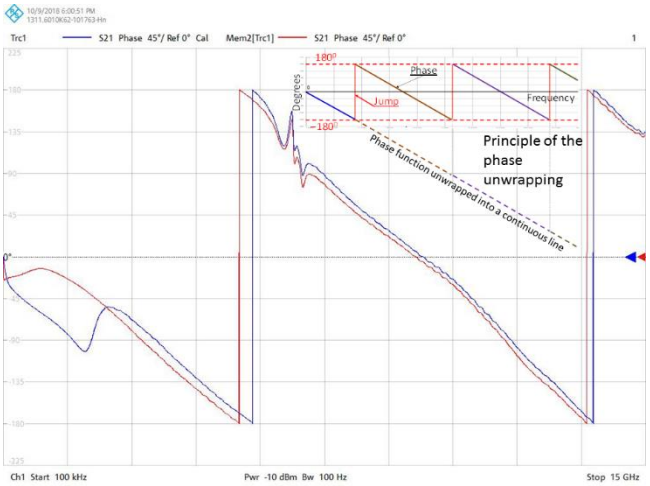

FIG. 2. The phase of $S_{21}(\omega)$ measured in a ferromagnetic wire at zero and a large magnetic field. The unwrapped phase at zero field and stress is used for calculating the delay time along the wire sample.

Thus, the delay time Δt caused by the wave propagation along the sample equals $|a|$. For the calculation of Z, $S_{21}(\omega)$ in the equation above must be replaced with $\bar{S}_{21}(\omega) =$

$S_{21}(\omega)\, exp(\, i\omega\Delta t)$, where i is the imaginary unit. In the proposed measurement technique, special care must be taken to minimize uncertainties associated with the contact pads on the microstrips for the wire sample. The dimension of the pads must be much smaller than the shortest wavelength propagating along the microstrips. Also, they must be much smaller than the gap for the wire sample thus minimising the phase uncertainties in the phase unwrapping technique.

For MI measurements, a DC offset voltage from FG is applied to the power amplifier to feed the Helmholtz coil. The actual voltage (after amplification) applied to the coil is measured by DMM. Its reading is passed to the program to be recalculated into the field using the coil calibration coefficient (field/voltage). After applying a DC offset voltage, the program is paused to allow the full coil charge/discharge during $>> L/R$, where L and R are the coil inductance and resistance respectively. After the pause (ms), VNA is activated to measure S_{21} in discrete frequency points in single sweep. The transmission coefficient measured in discrete frequency points is passed as an array to the LabVIEW program, where it is corrected to compensate the sample phase incursion and converted into the impedance. After the sweep, the measurement process is repeated with the next field point.

For SI measurements, between successive strain steps, in a single sweep VNA measures S_{21} in discrete frequency points over a wide range for a specified magnetic field as a bias. During this sweep, the displacement between the machine grippers is kept constant. Measuring the dispersion of S_{21} for a large number of bias fields and then transferring this data to PC may take several minutes. During this time, the local strain near the sample may slightly release due to viscous flow of PCB. For controlling the real strain applied to the sample, we used the digital imaging correlation technique (DIC) provided by LaVISION optical camera. With just a grey color scale for a pixel intensity, the digital camera creates a unique signature for each point of the image. A

point signature is correlated by neighboring points. When the image is being deformed, these point signatures move from their original positions revealing local vector displacements. The magnitude of a local displacement can be visualized using a 256-level color graduation (Fig. 1(a)). So, selecting a certain direction, the color mapping of the displacement spatial distribution along this direction can be created. For tracking a stretching of the gap, one needs to select some small reference areas at its edges. The program will automatically identify the reference points in these areas. When applying the tensile stress to the PCB board, the difference between the displacements of the reference points will give the absolute stretching of the gap.

Broadband magneto-impedance and stress-impedance measurements

In order to illustrate the developed technique for the MI and SI measurements in a wide frequency range, we used a glass-coated ferromagnetic wire with the alloy composition (wt%) $Co_{68.7}Fe_4Si_{11}B_{13}Ni_1Mo_{2.3}$ produced by the Taylor-Ulitovsky method.[14] The wire had a metal core diameter of 18.6 μm and total diameter of 21.6 μm. The sample gap in the dogbone cell was 25 mm. Fig. 3 shows characteristic features of the MI behavior measured at the MHz and GHz frequencies. For MHz frequencies, the impedance field dependencies have two symmetrical maximums within the field scanning range. Increasing the frequency, the impedance magnitude also increases. In the transition from the MHz to GHz frequencies, a rather complex scenario of changing of the MI curves is observed. Starting from some frequency in the upper MHz range (~700 MHz for the wire in Fig. 3), the inflection points will gradually develop on the MI curves before the maximums. Increasing the frequency further, the maximums will grow to a certain value and simultaneously shift to the region of larger fields, while the inflection points will reduce their impedance values. When the maximums already shifted outside the field scanning region, MI

curves will take shapes with two distinct slopes. Further increase in frequency will result in the slow slopes becoming almost the horizontal lines. This final shape will be saved for higher frequencies in the GHz range with further decrease of the impedance magnitude. These subtle transitions in magneto-impedance curves have not been accurately tracked in previous reports.

The behavior of MI shown in Fig. 3 can be qualitatively reproduced using the MI model proposed in Ref. 10. There, the magnetization vector $\overrightarrow{\boldsymbol{M}}_0$ of the homogeneously magnetized shell of the wire is rotated by the external magnetic field H_{ex} according to the Stoner-Wohlfarth model [15] with the density of magnetostatic energy $U(\varphi) = -M_0((H_K/2)\,cos^2(\alpha - \varphi) + H_{ex}\,cos(\varphi))$, where $\alpha \leq 90^0$ is the anisotropy angle measured from the wire axis, φ is the equilibrium angle of $\overrightarrow{\boldsymbol{M}}_0$ in the presence of H_{ex} ($\varphi = \alpha$ for $H_{ex} = 0$), $M_0 = |\overrightarrow{\boldsymbol{M}}_0|$, and H_K is the anisotropy field. The ac magnetic susceptibility, calculated from the Landau-Lifshitz equation, allows one to solve the Maxwell equations inside the wire and thus find the wire surface impedance tensor. One of its diagonal components can be expressed through the wire impedance Z as explained in the next section. The shape of the MI curves calculated in the frame of this model approach is very sensitive to the value of the spin-relaxation parameter, which should be chosen sufficiently small to reproduce the scenario of transformations shown in Fig. 3. The radial distribution of the magnetic properties might also contribute to the observed transformations. To solve these questions we require a separate research which will be conducted elsewhere. For now we have an accurate measurement technique that allows us to confidently discuss these effects.

The splitting of the MI curves observed at large positive fields after the full field scan (see Fig. 3), especially for 2 and 7 GHz is also another issue to take into consideration. These splits might be taken as measurement uncertainties, but most likely they are caused by the magnetization reversal processes in the inner core with the longitudinal magnetization. The conductivity through

the inner core has never been included into the previous MI models. Measurements of MI in larger magnetic fields might clarify this question.

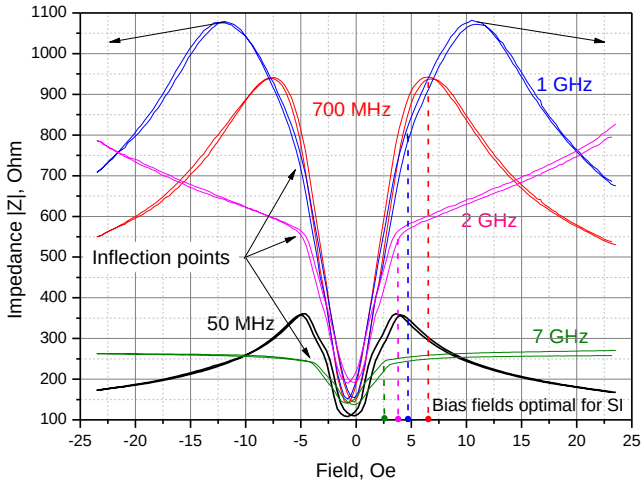

FIG. 3. Field dependencies of the impedance in the MHz and GHz ranges. A complex scenario of changing of the MI curves has been revealed in the transition from the MHz to GHz frequencies.

The same as MI, the stress sensitivity of the impedance is due to the rotation of the magnetization in the circularly magnetized shell of the wire. Staying within the Stoner-Wohlfarth magnetostatic model, the anisotropy field H_K of the shell can be expressed through the total tensile stress $\sigma = \sigma_{res} + \sigma_{ex}$ applied to the wire: $H_K = 3\lambda\sigma/M_0$, where σ_{res} is the residual tensile stress induced during the wire casting process, σ_{ex} is the external tensile stress, and λ is the magnetostriction constant. Since the maximums of MI occur at $H_{ex} = \pm H_K$, applying an external tensile stress will result in widening of the MI curves, while the impedance in zero bias field will remain unchanged for any frequency as shown in Fig. 4. Thus, to realize SI behavior in a wire with a circumferential anisotropy, an external magnetic bias field must be applied. The complex scenario of MI change in the transition from the MHz to GHz ranges revealed in Fig. 3 enables the

selection of the optimal frequency-dependent bias field. In the MHz range, it must be taken at the maximums of MI, while in the GHz range at the inflection points.

The parasitic resonances observed between 6 and 7 GHz were introduced during the SOLT calibration and are caused by the OPEN terminations on the PCB calibration cell. These resonances are well localized and can be easily replaced with smooth interpolants.

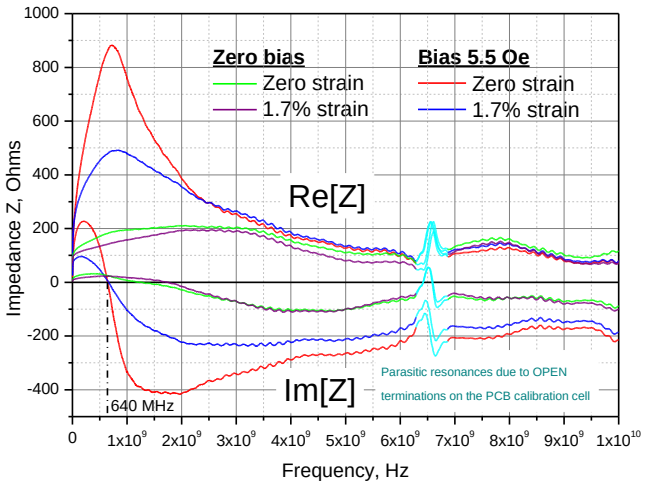

FIG. 4. Stress dependence of the dispersion of the real and imaginary impedances. The bias field 5.5 Oe was optimal for 640 MHz close to the ferromagnetic resonance.

The strongest stress sensitivity of the impedance should be expected at the ferromagnetic resonance. In Fig. 5, SI was measured at 640 MHz, close to the resonance, at different bias fields. At zero bias, the wire is almost stress insensitive (see also Fig. 4). The optimal bias field for this frequency was 5.5 Oe providing a full impedance change of more than 350 Ω for 1.7% strain. Thus, the maximum SI effect for the chosen wire is 41% calculated with respect to the maximum impedance value at zero strain. Applying larger bias fields, the stress sensitive interval will be shifted toward higher strains. For these particular frequency (640 MHz) and bias field (5.5 Oe), the stress sensitivity comes mostly from the real part of the impedance. In general, both the real

and imaginary parts will be stress sensitive in a wide range around the resonance. On the contrary, for higher GHz frequencies, SI is caused mostly by the imaginary part as can be noticed in Fig. 4. Having in mind remote stress sensing applications, it would be important to have a sufficiently large SI at higher GHz frequencies, where the dimensions of the measurement components, e.g. a lens horn antenna or waveguide open end, can be significantly reduced. Fig. 6 shows SI at 7 GHz where the change in total impedance was 27% at 2.5 Oe. The optimal bias field 2.5 Oe was chosen in accordance with MI behavior at 7 GHz in Fig. 3.

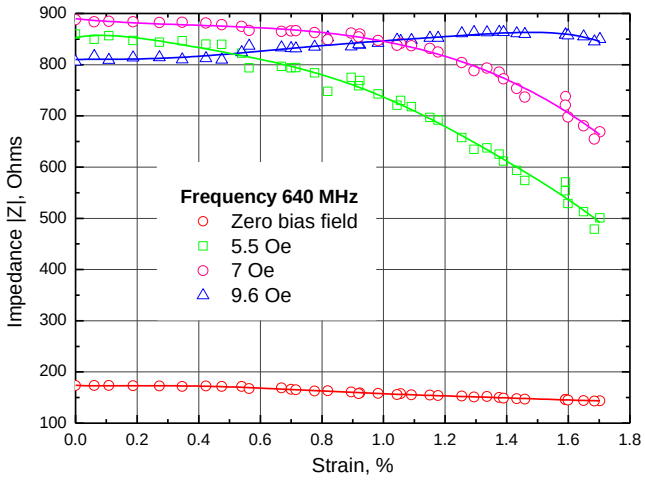

FIG. 5. Stress impedance measured at 640 MHz, close to the ferromagnetic resonance, and different bias fields. The highest stress sensitivity was achieved at the bias field 5.5 Oe.

Published: Measurement Science and Technology **31**, p. 025901 (2020) DOI: 10.1088/1361-6501/ab4556

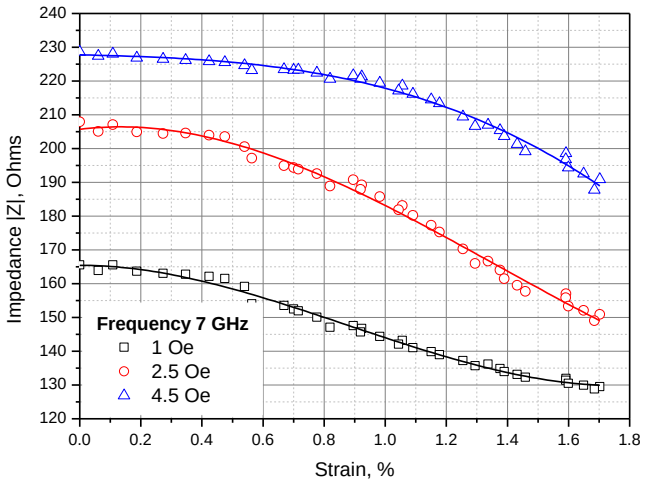

FIG. 6. Stress impedance measured at 7 GHz and different bias fields. The highest stress sensitivity was achieved at the bias field 2.5 Oe.

Operation frequencies in the GHz range are hardly of practical interest for the impedance sensor elements incorporated into electronic circuits. However, new possibilities open up if using remote microwave sensing. In this case, higher frequencies would be required to provide compact microwave design and smaller irradiation spot, e.g. if using a horn antenna with the focusing lens or a waveguide with the open end.

For stress monitoring applications, a composite surface could be remotely interrogated by measuring the reflection coefficient in the near-field region when it is exposed to the focused electromagnetic radiation from a lens horn antenna or waveguide open end. Applying such insignificant fields within the spot of exposure of electromagnetic wave is not an issue and can be realized by means of a net of parallel currents placed on surface. In laboratory conditions, the transmission coefficient can also be measured. However, the main problems of remote stress monitoring will be associated with the calibration of antenna measurements as well as their

Published: Measurement Science and Technology **31**, p. 025901 (2020) DOI: 10.1088/1361-6501/ab4556

interpretation in terms of the distribution of local stress. Without an accurate description of the microscopic scattering properties of wire inclusions, such an interpretation would be impossible.

Therefore, we proceed now to discuss the formalism to find the impedance boundary condition required for the antenna equation which will allow us to describe the microwave scattering properties.

Published: Measurement Science and Technology **31**, p. 025901 (2020) DOI: 10.1088/1361-6501/ab4556

Surface impedance boundary condition for the antenna equation

For the current I induced by a voltage V applied across a wire, the circular magnetic field on the wire surface is (cgs units) $\bar{h}_\varphi = 2I/(ac) = 2V/(Zac) = \bar{e}_z 2l/(Zac)$, where a is wire radius, c is the speed of light, $\bar{e}_z$ electrical field on the wire surface, and l is the wire length. The coefficient $\xi_{zz} = \bar{e}_z/\bar{h}_\varphi = Zac/(2l)$ is called the longitudinal surface impedance, one of four components of the surface impedance tensor.[10] It can be expressed through the impedance Z measured in Ohms: $\xi_{zz}^{\text{cgs}} = 10^9(a/l)Z[\Omega]/(2c)$, where $c \approx 3 \times 10^{10}$ cm/s. This parameter includes all information about both conductive and magnetic properties. The surface impedance ξ_{zz} along with the dielectric constant ε of the surrounding medium are the only material parameters in the integro-differential equation ("antenna equation") describing the current distribution induced in a wire irradiated by an electromagnetic wave (cgs units):[7] $\frac{d^2(G*j)}{d^2z} + k^2(G*j) = \frac{i\omega\varepsilon\bar{e}_z}{(4\pi)} - \frac{i\omega\varepsilon\xi_{zz}(G_\phi*j)}{(2\pi ac)}$. In the antenna equation approach, the induced wire current is modelled by the volume current density $j(z)\delta_S(x,y)$, where $j(z)$ is the linear current density and $\delta_S(x,y)$ is two dimensional Dirac's function. With respect to the other quantities in the antenna equation, $(G*j) = \int_{-l/2}^{l/2} j(s)G(r)ds$ is the convolution with $G(r) = exp(ikr)/(4\pi r)$, $r = \sqrt{(z-s)^2 + a^2}$, $k = (\omega/c)\sqrt{\varepsilon}$ is the wave number, $(G_\phi * j) = \int_{-l/2}^{l/2} j(s)G_\phi(r)ds$ is the convolution with $G_\phi = a^2(1-ikr)\,exp(ikr)/(2r^3)$, and $\bar{e}_z$ is the projection of the electric field in the electromagnetic wave onto the microwire axis. In the obliquely incident wave, $\bar{e}_z$ will be a periodical function of z.

Conclusions

In summary, we have developed a measurement technique, including PCB measurement and calibration cells, which allowed broadband impedance measurements in the presence of both magnetic field and tensile stress stimuli. The robust experimental setup enabled us to identify magneto-impedance transformations at different frequencies that cannot be explained within the framework of existing models and that until now have not been accurately tracked. Moreover, the contribution of both real and imaginary impedance to the stress sensitivity in MHz and GHz regimes was also disclosed. The measured dispersion of the wire impedance can be then recalculated into the surface impedance which constitutes the boundary condition in the antenna equation describing a wire scatterer in terms of the linear current density induced by the incident electromagnetic wave. Our approach constitutes the basis for predictive modeling of microwave properties and rigorous scattering theories in such wire composites using accurately measured wire material properties.

Acknowledgements

This work was supported by NSFC No. 51671171, and No. 51811530103; Basic Funding for Central Universities No. 2018QNA4001. Qin is indebted to the support of the *"National Youth Thousand Talent Program"* of China. The results of this work were presented at Zwick Roell Science Award 2018 and won the bronze medal. We gratefully acknowledge the support from Zwick Roell for providing the stress machine and encouraging high quality research.

References

[1] Tejedor M, Hernando B, Sánchez M L, et al. 2000 Magneto-impedance effect in amorphous ribbons for stress sensor application *Sens Actuators A* **81** 98-101.

[2] Ipatov M, Zhukova V, Zhukov A, et al. 2013 Expanding the longitudinal magnetoimpedance sensor range by direct bias current *J Appl Phys* **113** 351-6.

[3] Mohri K, Uchiyama T, Shen L P, et al. 1998 Amorphous wire & CMOS IC based sensitive micro magnetic sensors utilizing magneto-impedance (MI) and stress-impedance (SI) effects and applications I*EEE Trans Magn* **38** 3063-8.

[4] Olivera J, González M, Fuente J V, et al. 2014 An Embedded Stress Sensor for Concrete SHM Based on Amorphous Ferromagnetic Microwires *Sensors* **14** 19963-78.

[5] Qin F X, Peng H X, Phan M H, Panina L V, Ipatov M, and Zhukov A 2012 Effects of wire properties on the field-tunable behaviour of continuous-microwire composites *Sens Actuators A* **178** 118

[6] Qin F X, Peng H X 2013 Ferromagnetic microwires enabled multifunctional composite materials *Prog Mater Sci* **58** 183-259.

[7] Peng H X, Qin F X and Phan M H 2016 Giant Magnetoimpedance Sensors and Their Applications. *Ferromagnetic Microwire Composite* (Springer, Cham.) pp. 99-117.

[8] Makhnovskiy D P, Panina L V 2003 Field dependent permittivity of composite materials containing ferromagnetic wires[J] *J Appl Phys* **93** 4120-9.

[9] Ipatov M, Aranda G R, Zhukova V, Panina L V, González J and Zhukov A 2011 Tunable effective permittivity of composites based on ferromagnetic microwires with high magneto-impedance effect *Appl. Phys. A* **103** 693.

[10] Makhnovskiy D P, Panina L V, Garcia C, Zhukov A P and Gonzalez J 2006 Experimental

demonstration of tunable scattering spectra at microwave frequencies in composite media containing CoFeCrSiB glass-coated amorphous ferromagnetic wires and comparison with theory *Phys. Rev. B* **74** 064205.

[11] Liberal I, Nefedov I S, Ederra I, et al. 2011 Electromagnetic response and homogenization of grids of ferromagnetic microwires *J. Appl. Phys* **110** 2066.

[12] Reynet O, Adenot A L, Deprot S, et al. 2002 Effect of the magnetic properties of the inclusions on the high-frequency dielectric response of diluted composites *Phys. Rev. B* **66** 94412.

[13] Hiebel M 2008 Design of a heterodyne N-port network analyzer. Fundamentals of Vector Network Analysis, 4th ed *Rohde & Schwarz GmbH & Co.: Munich, Germany* 22-79.

[14] Larin V S, Torcunov A V, Zhukov A, Vazquez M and Panina L 2002 Preparation and properties of glass-coated microwires *J. Mag. Magn. Mater* **249** 39

[15] Aharoni A 2000 *Introduction to the Theory of Ferromagnetism* (Clarendon Press) Vol. 109